A Method for Detecting Lagrangian Coherent Structures (LCSs) using Fixed Wing Unmanned Aircraft System (UAS)

Peter J. Nolan[1], Hunter McClelland[2], Craig Woolsey[2], Shane D. Ross[1]

[1] Department of Biomedical Engineering and Mechanics, Virginia Tech, Blacksburg, VA, USA; pnolan86@vt.edu, sdross@vt.edu
[2] Kevin T. Crofton Department of Aerospace and Ocean Engineering, Virginia Tech, Blacksburg, VA, USA; hgm@vt.edu, cwoolsey@vt.edu

Contact: pnolan86@vt.edu

Abstract

TBD

1 Introduction

The transport of material in the atmosphere is a problem with important implications for agriculture [1–4], aviation [5, 6], and human health [7, 8]. Given the turbulent nature of the atmosphere it can be difficult to predict where a particle, such as a plant pathogen, will wind up. Tools from dynamical systems theory, such as LCSs, can help us to understand how particles in a flow will evolve. The study of transport in the atmosphere from a dynamical systems perspective has long focused on the study of large scale phenomena [1–5, 9–12]. This has been largely due to the larger scale grid spacing of readily available atmospheric model data and the lack of high resolution atmospheric measurements on a scale large enough to calculate Lagrangian data. Furthermore, few works have attempted to find ways to detect LCSs in the field. In [6, 13] the authors used wind velocity measurements from a dopler LiDAR to detect LCS which had passed through Hong Kong International Airport. The authors in [1] took a different, rather than measure the wind velocity to try and detect LCSs, the authors looked at sudden changes in pathogen concentrations in the atmosphere and were able to link those changes to the passage of LCSs using atmospheric forecasts from the North American Mesoscale (NAM) model. Yet to date, we are unaware of any attempts to develop a means of directly sense LCSs in which could be readily implemented by operators in the field. Recent advances in dynamical systems theory, such as new Eulerian diagnostics, as well as, atmospheric sensing technology, such as unmanned aircraft systems (UAS), have brought the detection of localized LCSs within reach.

The first of these developments are new Eulerian techniques for measuring the attraction and repulsion of regions in a fluid flow [14, 15]. In traditional Lagrangian analyses a velocity field is needed which is defined over a large enough spatiotemporal scale for the advection of virtual particles. These new Eulerian methods do not rely on the advection of virtual particles, instead they utilize the gradients of the velocity field. Since they rely on gradients, these techniques we only require enough points to enact a finite-differencing scheme. Furthermore, these methods are Eulerian and thus can be made using temporally coarse or even temporally pointwise data sets.

The second of these developments is the use of inexpensive UAS to sample the atmospheric velocity instead of piloted aircraft or other traditional assets. Ground-based wind sensors such as LiDAR (light detection and ranging), SoDAR (sonic detection and ranging), or tower-mounted anemometers can be prohibitively expensive and difficult to relocate to regions of interest, such as a hazardous zone. Airborne wind measurement from aircraft has a long history [16, 17] and well-developed existing programs [18]. The proliferation of unmanned aircraft systems (UAS) has enabled wind measurement missions which may be lower cost, longer duration, or in more dangerous environments. Elston et. al. [19] provide a review of many UAS atmospheric measurement efforts, and recent works continue to advance both theoretical and practical UAS capabilities [20–25].

In this paper we will take advantage of these developments to advance a methodology, based on numerical simulations, which will enable UAS operators in the field to utilize their wind measurements to detect LCSs.

2 Methods

2.1 Lagrangian-Eulerian Analysis

We will be analyzing the dynamical system

$$\frac{d}{dt}\mathbf{x}(t) = \mathbf{v}(\mathbf{x}(t), t), \tag{1}$$

$$\mathbf{x}_0 = \mathbf{x}(t_0). \tag{2}$$

In this system $\mathbf{x}(t)$ is the position vector of a fluid parcel at time t and $\mathbf{v}(\mathbf{x}, t)$ is the horizontal wind velocity vector at position $\mathbf{x}(t)$, time t. We define the components of the horizontal position vector, $\mathbf{x} = (x, y)$, where x is the eastward position and y is the northward position and the horizontal velocity vector, $\mathbf{v} = (u, v)$, where u is the eastward velocity and v is the northward velocity.

We will be analyzing this system using both Langrangian and Eulerian tools. For the Lagrangian analysis we will be using the Finite-Time Lyapunov Exponent (FTLE), σ, and Lagrangian coherent structures (LCSs). We define LCSs as C-ridges of the FTLE field following [26]. The FTLE field is a measure of the stretching of a fluid parcels within a flow, the forward-time FTLE measures repulsion and the backward-time FTLE measures attraction. LCSs on the other hand are the most attracting and repelling material surfaces within a fluid flow; they provide a means of visualizing how particles within the flow will evolve.

For the Eulerian analyses we use the attraction rate, s_1, and the trajectory divergence rate, $\dot{\rho}$, both of which are derived from the Eulerian rate-of-strain tensor, $\mathbf{S}$, described in equation 6. The attraction rate is the minimum eigenvalue of $\mathbf{S}$ and was shown in ref [14] to provide a measure of instantaneous hyperbolic attraction, with isolated minima of s_1 providing the cores of attracting objective Eulerian coherent structures (OECS). Recent work has shown that in 2D, s_1 is the limit of the backward-time FTLE as integration time goes to 0 [27]. The trajectory divergence rate is a measure of how the how much repulsion is changing along streamlines of the velocity field.

To calculate Lagrangian metrics we must first calculate the flow map for the time period of interest,

$$\mathbf{F}_{t_0}^{t}(\mathbf{x}_0) = \mathbf{x}_0 + \int_{t_0}^{t} \mathbf{v}(\mathbf{x}(t), t)\, dt. \tag{3}$$

Taking the gradient of the flow map we can then calculate the right Cauchy-Green strain tensor,

$$\mathbf{C}_{t_0}^t(\mathbf{x}_0) = \nabla\mathbf{F}_{t_0}^t(\mathbf{x}_0)^T \cdot \nabla\mathbf{F}_{t_0}^t(\mathbf{x}_0), \tag{4}$$

From the largest eigenvalue of the right Cauchy-Green strain tensor, λ_n, we can then calculate the FTLE field,

$$\sigma_{t_0}^t(\mathbf{x}_0) = \frac{1}{2|t-t_0|}\log\left(\lambda_n(\mathbf{x}_0)\right) \tag{5}$$

For the Eulerian metrics, the Eulerian rate-of-strain tensor is defined as

$$\mathbf{S}(\mathbf{x}_0) = \frac{1}{2}\left(\nabla\mathbf{v}(\mathbf{x}_0) + \nabla\mathbf{v}(\mathbf{x}_0)^T\right). \tag{6}$$

The attraction rate, s_1, is the minimum eigenvalue of $\mathbf{S}$. The trajectory divergence rate is defined as

$$\dot{\rho}(\mathbf{x}_0) = \hat{\mathbf{n}}(\mathbf{x}_0)^T \cdot \mathbf{S}(\mathbf{x}_0) \cdot \hat{\mathbf{n}}(\mathbf{x}_0) = \frac{1}{||\mathbf{v}(\mathbf{x}_0)||^2}(\mathbf{v}(\mathbf{x}_0)^T \cdot \mathbf{J}^T \cdot \mathbf{S}(\mathbf{x}_0) \cdot \mathbf{J} \cdot \mathbf{v}(\mathbf{x}_0)), \tag{7}$$

where $\hat{\mathbf{n}}(\mathbf{x}_0)$ is the unit vector normal to the trajectory and $\mathbf{J}$ is the symplectic matrix [15]. A visual interpretation of the trajectory divergence rate can be found in figure 1.

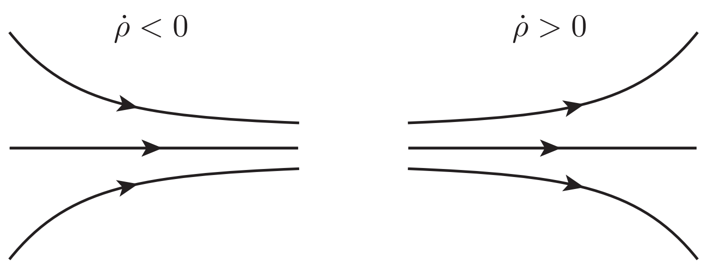

Figure 1: Schematic of the trajectory divergence rate, taken from [15]. Where $\dot{\rho} < 0$, trajectories are converging, where $\dot{\rho} > 0$ trajectories are diverging.

2.2 Gradient Approximation from UAS Flight Data

In order to calculate the Eulerian rate-of-strain tensor from our UAS data sets we have developed an algorithm to calculate the gradient of a scalar field based on measurements along a circular arc. An assumption that goes into this algorithm is that the scalar field is not significantly changing in time during the period of one full orbit, but is changing in space. We believe this assumption is appropriate to apply to atmospheric velocity fields, as mid to larger scale atmospheric flows tend to change on the order of hours, while UAS orbits are on the order of minutes. This assumption of course ignores small scale turbulent motion which would fall below the scale at which we are sampling, m vs km. This algorithm also assumes that the important features will be in the horizontal plane. This assumption was previously applied to atmospheric model data in [9, 10, 28] based on the fact that the vertical component of the wind velocity tends to be two orders of magnitude less than the horizontal components.

This algorithm takes the radius of the circle, r, which is assumed to be constant, as a scalar input, the angle θ as an $n \times 1$ array input, and a scalar u as an $n \times 1$ array input. Note, this algorithm is currently written for a clockwise trajectory, however, it would work equally well for a counterclockwise trajectory with the appropriate modifications. We start with an initial point along the circular flight path (r, θ_0) an u at that point, then provided the path continues for at least another $\frac{3}{4}$ of a circle, interpolate u to 3 additional points along the path at $(r, \theta_0 - \frac{1}{2}\pi)$, $(r, \theta_0 - \pi)$, and $(r, \theta_0 - \frac{4}{3}\pi)$. With u at 4 individual points along the flight path use a central difference scheme to approximate the gradient of u at the center point of the circular path. Since these 4 points are along an arc, the gradient of each set of 4 points will be in a different frame of reference from our initial set. To correct for this we apply a counterclockwise rotation to the gradient vector of u to obtain the gradient in our reference frame. Continue this method for each additional point along the circular path until there is less then an additional $\frac{3}{4}$ of a circle left. A pseudo-code version of this algorithm can be found in Algorithm 1, and a schematic can be found in figure 2.

2.3 Model Data

For a velocity field we used data from the 3km North American Mesoscale (NAM) model. We looked at a section of the model over Southwestern Vir-

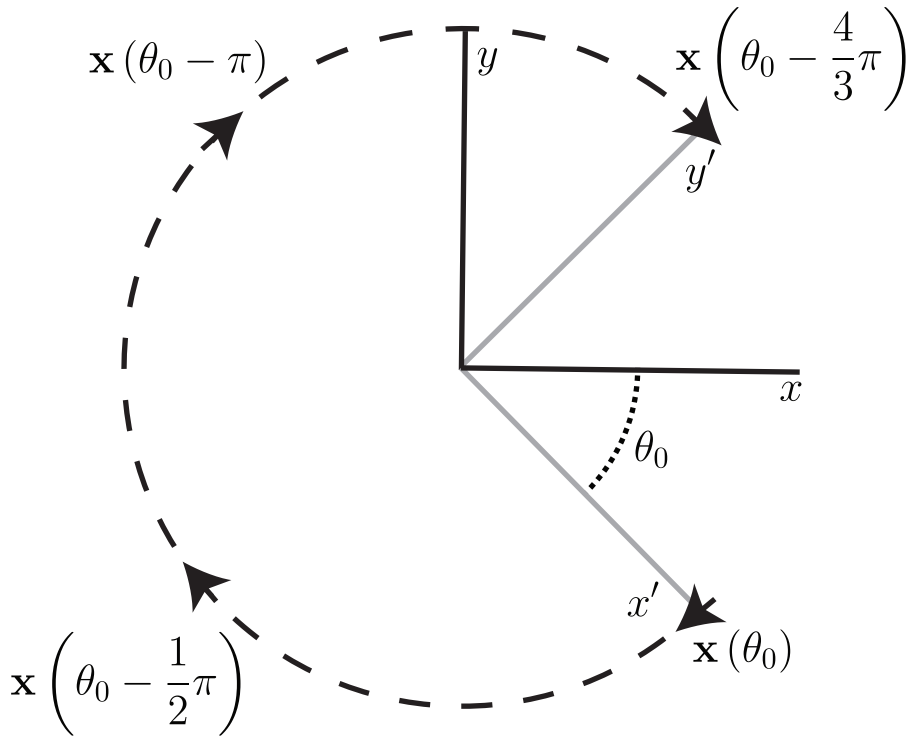

Figure 2: Schematic showing positions where velocity measurements were made and the position of the circle gradient frame to the reference frame.

ginia centered at the Virginia tech experimental farm during a 215hr period beginning Sept 4^{th}, 2017 at 00:00 UTC. We divided the NAM data was into 2 parts. The first part was a strictly 2D data set that looked at the 850mb isosurface, the second was a 3D data set. Both data sets were interpolated in time from 1hr resolution to 10min resolution using cubic splines. The 3D data was then interpolated from pressure based vertical levels to height based vertical levels using linear interpolation from MATLAB's scatteredInterpolant routine. Both data sets were also interpolated from a 3km horizontal resolution to a 300m horizontal resolution using cubic Lagrange polynomials. The 3D data set was then fed to a flight simulator which attempted the follow the 850mb isosurface. A subscale model of a transport-style aircraft, named the T-2, was used as the simulated unmanned aircraft. To get a sense of its scale, some of its common physical properties are

$$\text{mass } m = 22.5 \text{ kg} \qquad \text{wingspan } b = 2.09 \text{ m} \qquad \text{chord } \bar{c} = 0.28 \text{ m}$$

Algorithm 1 Circle Gradient

input $\theta, u(\theta), r$
for i in length(θ) **do**
  if $\theta(i) - \frac{4}{3}\pi \geq \theta(\text{end})$ **then**
    interpolate $u(\theta)$ to $u\left(\theta(i) - \frac{1}{2}\pi\right), u\left(\theta(i) - \pi\right), u\left(\theta(i) - \frac{4}{3}\pi\right)$
    $\frac{du}{dx'} = \frac{u(\theta(i)) - u(\theta(i) - \pi)}{2 \cdot r}$
    $\frac{du}{dy'} = \frac{u\left(\theta(i) - \frac{1}{2}\pi\right) - u\left(\theta(i) - \frac{4}{3}\pi\right)}{2 \cdot r}$
    $\nabla u(i) = \begin{bmatrix} cos(\theta(i)) & sin(\theta(i)) \\ -sin(\theta(i)) & cos(\theta(i)) \end{bmatrix} \begin{bmatrix} \frac{du}{dx'} \\ \frac{du}{dy'} \end{bmatrix}$
return ∇u

The T-2 cruising airspeed is approximately 40 m/s. The details of the flight dynamic model are included in Appendix A. The simulated wind "measurements" taken by the aircraft are wind field components along the aircraft's center-of-mass trajectory $\mathbf{v}(\mathbf{x}(t), t)$.

3 Results and Discussion

3.1 Approximating local Eulerian Metrics from UAS flights

In this section we examine how well the attraction rate, s_1, and the trajectory divergence rate, $\dot{\rho}$, can be approximated from a UAS flight. Figure 3 shows the results for the trajectory divergence rate. Using the 850mb isosurface velocity field we calculated the trajectory divergence rate at the center point of our circle/flight radius, shown in red. We then used velocity data from a perfectly circular path with a radius varying from 2km to 15km restricted to the 850mb isosurface to approximate the trajectory divergence rate, shown in black. Finally, we used velocity data from a 3D simulated UAS flight path with a radius varying from 2km to 15km attempting to follow the 850mb isosurface to approximate the trajectory divergence rate, shown in blue. Pearson correlation coefficients for these measurements can be found in table 3.1.

We can see from the results in figure 3 that the simulated UAS flight in a 3D space provides a very similar result to the circular path restricted to the 850mb isosurface. For all the radii we looked at the trajectory divergence

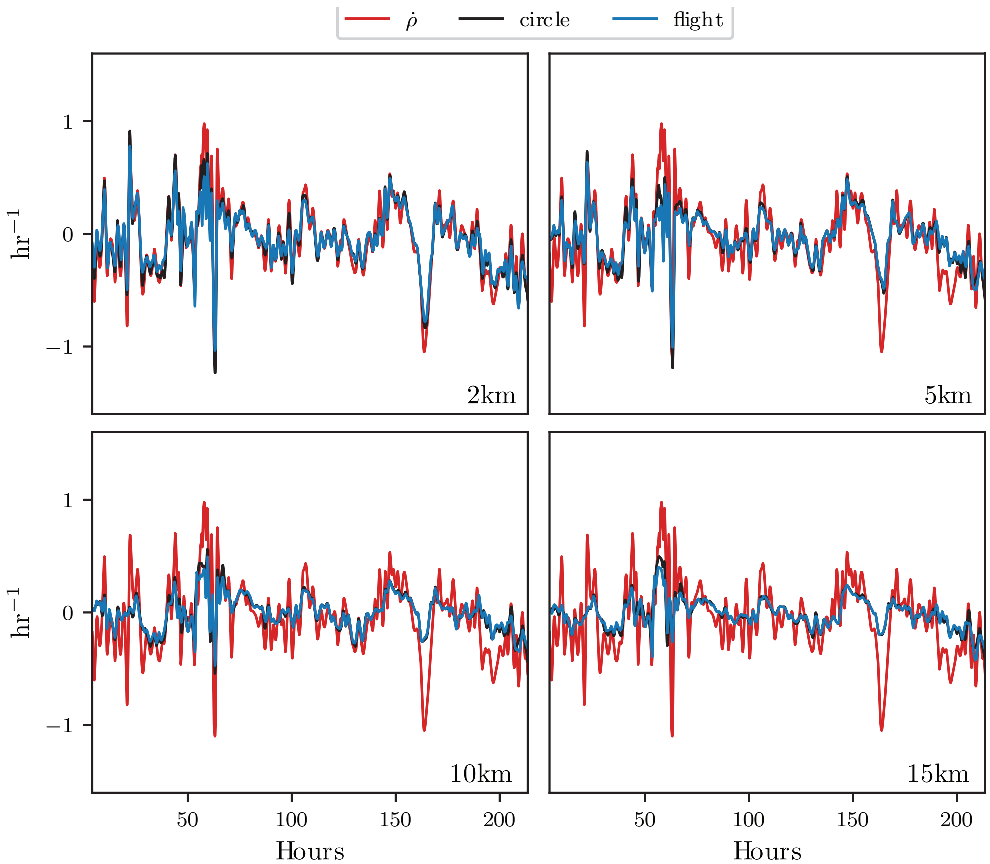

Figure 3: Comparison of the trajectory divergence rate measurements between center point (red), circular arc (black), and simulated drone flight (blue). Radius for the measurements is shown in lower right hand corner.

rate from the flight simulation is nearly identical to that from the 2D circular path. Most of the error between the center point trajectory divergence rate and the estimate from our 3D flights appears to be due to the distance from the point of estimation, rather than inconsistencies in the flights path due to buffeting. This can also be seen in table 3.1, where the correlation coefficients between the simulated flight and the 2D circle are all > 0.95, while we see a steady drop in the correlation coefficients with the center point trajectory divergence rate as the radius increases.

Figure 4 shows the results for the attraction rate. Using data from the 850mb isosurface we calculated the attraction rate at the center point of our

	2km circle	5km circle	10km circle	15km circle	2km flight	5km flight	10km flight	15km flight
center point	0.955	0.854	0.790	0.730	0.931	0.827	0.781	0.730
2km circle	--	0.946	0.815	0.751	0.981	0.923	0.811	0.765
5km circle		--	0.866	0.768	0.935	0.981	0.865	0.784
10km circle			--	0.928	0.804	0.836	0.974	0.902
15km circle				--	0.745	0.738	0.904	0.955
2km flight					--	0.944	0.824	0.783
5km flight						--	0.870	0.793
10km flight							--	0.937

Table 1: Pearson correlation coefficients for $\dot{\rho}$ measurements. Coefficients range from 0.730 to 0.965.

	2km circle	5km circle	10km circle	15km circle	2km flight	5km flight	10km flight	15km flight
center point	0.939	0.838	0.677	0.590	0.910	0.821	0.675	0.577
2km circle	--	0.932	0.742	0.644	0.980	0.917	0.739	0.627
5km circle		--	0.898	0.789	0.916	0.980	0.887	0.760
10km circle			--	0.908	0.729	0.881	0.978	0.864
15km circle				--	0.637	0.788	0.907	0.965
2km flight					--	0.936	0.746	0.644
5km flight						--	0.900	0.791
10km flight							--	0.909

Table 2: Pearson correlation coefficients for attraction rate measurements. Coefficients range from 0.577 to 0.939.

circle/flight radius, shown in red. We then used velocity data from a perfectly circular path with a radius varying from 2km to 15km restricted to the 850mb isosurface to approximate the attraction rate, shown in black. Finally, we used velocity data from a 3D simulated UAS flight path with a radius varying from 2km to 15km attempting to follow the 850mb isosurface to approximate the attraction rate, shown in blue. Pearson correlation coefficients for these measurements can be found in table 3.1.

We can see from the results in figure 4 that the simulated UAS flight in a 3D space provides a very similar attraction rate measurements to the circular path restricted to the 850mb isosurface. For all the radii paths we looked at the attraction rate from the flight simulation is nearly identical to that from the 2D circular path. Most of the error between the center point attraction rate and the estimate from our 3D flights is due to the distance from the point of estimation, rather than inconsistencies in the flights path due to buffeting. This can also be seen in table 3.1, where the correlation coefficients between the simulated flight and the 2D circle are all > 0.96, while we see a steep drop in the correlation coefficients with the center point attraction rate as the radius increases.

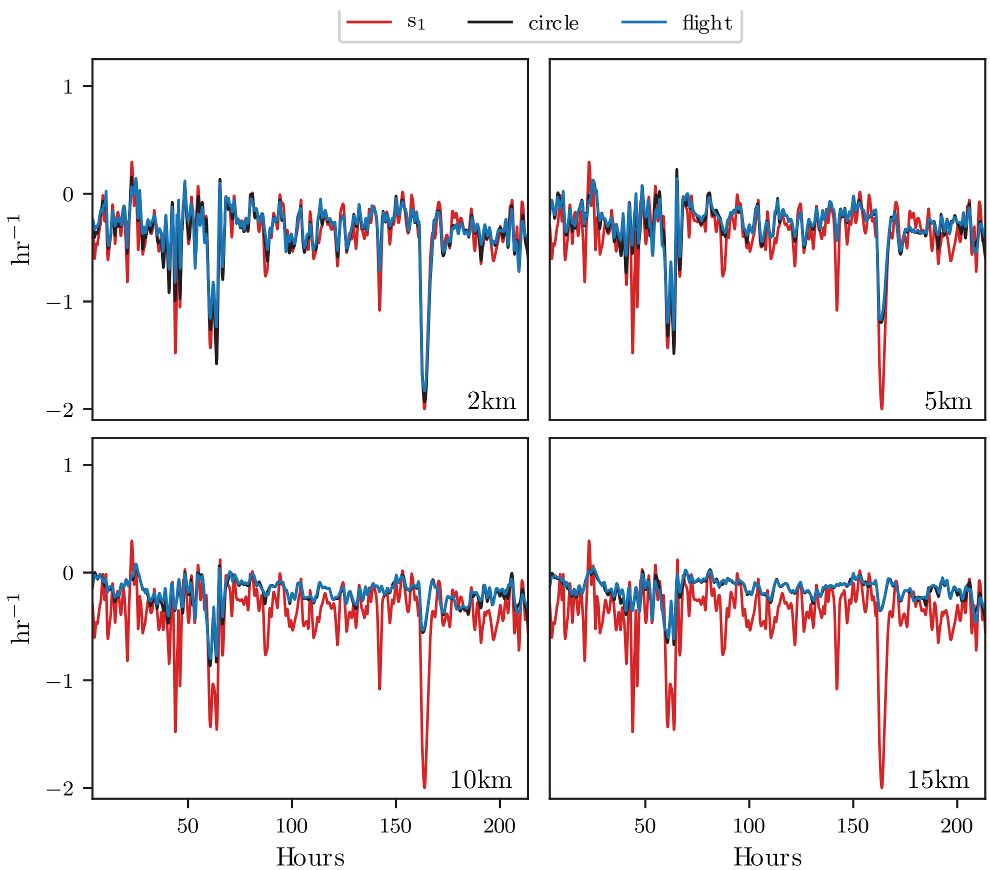

Figure 4: Comparison of the attraction rate measurements between center point (red), circular arc (black), and simulated drone flight (blue). Radius for the measurements is shown in lower right hand corner.

Both the attraction rate and the trajectory divergence rate at a point can be approximated to a high degree of accuracy by UAS flights. Simulated 3D UAS flights provided measurements which were nearly identical to those of perfect circular 2D paths. The main cause of error in the approximations appears to be the distance of the path from the center point. Furthermore, the trajectory divergence rate appears to be a more robust metric than the attraction rate; meaning that the trajectory divergence rate can be better approximated at larger radii than the attraction rate can. This can be seen very clearly seen in tables 1 and 2, where the correlation coefficient for the attraction rate drops off much quicker than for the trajectory divergence rate.

3.2 Using Eulerian Metrics to infer Lagrangian Dynamics

In this section we examine how well the attraction rate, s_1, and the trajectory divergence rate, $\dot{\rho}$, do at predicting Lagrangian dynamics, such as the passage of LCSs. Figure 5 shows the time series for the trajectory divergence rate and backward-time FTLE for integration times of 0.5, 1, and 2 hrs. The FTLE values have been multiplied by -1 for improved visualization. In this figure we can see that the trajectory divergence rate does not always follow the trend of the negative backward-time FTLE, which is to be expected. The trajectory divergence rate gives information on both instantaneous attraction and repulsion, while the negative backward-time FTLE gives a measure of attraction. The trajectory divergence rate does, however, agree with the negative backward-time FTLE when we have significant periods of attraction. This behavior is of particular interest for the detection of LCSs. When calculating LCSs, there is often a multitude of weaker, less important LCSs. In order to filter out these less important structures and focus on important structures, one often needs to set a threshold value for the FTLE field. These dips in the the trajectory divergence rate, coinciding with the strongest dips in the negative backward-time FTLE, would therefore seem to be a likely indicator of LCS of interest.

Figure 6 shows the time series for the attraction rate and backward-time FTLE for integration times of 0.5, 1, and 2 hrs. The FTLE values have been multiplied by -1 for improved visualization. In this figure we can see that the attraction rate follows the general trend of the negative backward-time FTLE. This makes sense as both the attraction rate and the negative backward-time FTLE give measures of attraction. The attraction rate therefore, should give a good approximation to the negative backward-time FTLE, and thus should be able to give indications of LCSs.

We can further explore the effectiveness of the attraction rate and the trajectory divergence rate for detecting LCSs by looking at receiver operating characteristic (ROC) curves. For this we looked at when LCSs passed within a threshold radius which ranged from 400m to 10km of our center point, figure 7. We further applied a threshold of 90% for the LCSs, so only LCSs whose FTLE value was within the 90^{th} percentile were considered. We looked at the attraction rate's and the trajectory divergence rate's ability to detect LCSs for integration times of $\frac{1}{2}, 1$, and 2 hrs in backward-time.

Figure 8 show ROC curves for the the trajectory divergence rate. The

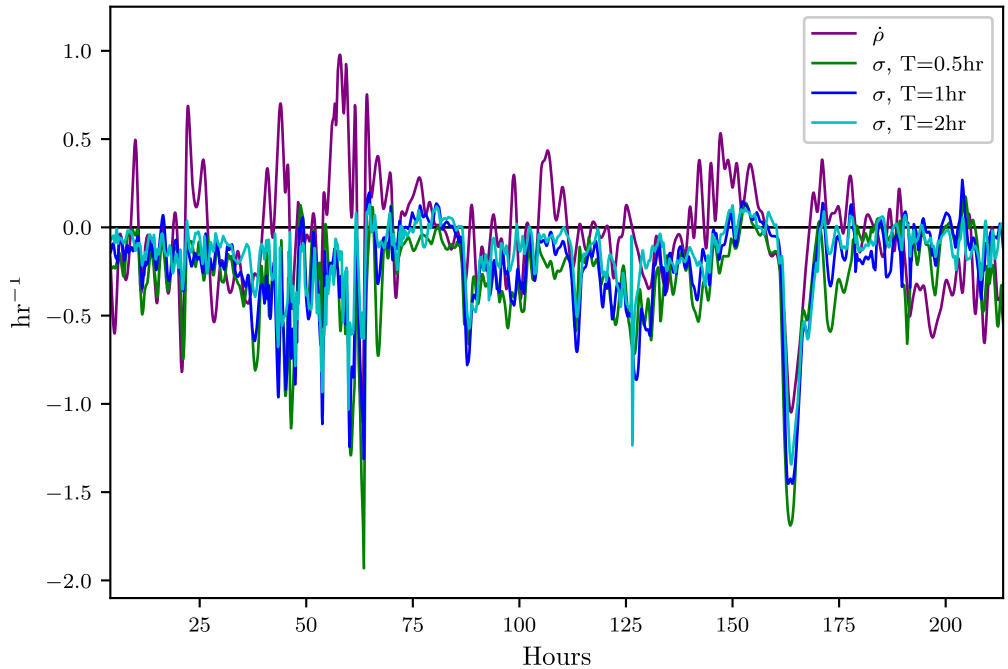

Figure 5: Comparison of the trajectory divergence rate with the 0.5, 1, and 2 hr backward-time FTLE from t=4 to t=215hrs. FTLE fields have been multiplied by -1 to offer better comparison of attraction.

trajectory divergence rate gives measures of both attraction and repulsion, so to filter out repulsive indicators we first masked trajectory divergence rate values > 0. After this, we threshold the from 0%, upper right hand side, to 100%, lower left hand corner. Every 20^{th} percentile is marked with a dot. Each subplot represents a different threshold radius, with radii ranging from 400m to 10km. Each color represents a different integration time for the LCSs, 0.5hr green, 1hr red, 2hr blue. These ROC curves indicate that the trajectory divergence rate can indeed be used to detect LCSs passing through an area.

Figure 9 shows ROC curves for the attraction rate. We threshold the attraction rate from 0%, upper right hand corner, to 100%, lower left hand corner. Every 20^{th} percentile is marked with a dot. Each subplot represents a different threshold radius, with radii ranging from 400m to 10km. Each color represents a different integration time for the LCSs, 0.5hr green, 1hr red, 2hr blue. These ROC curves indicate that not only can the attraction

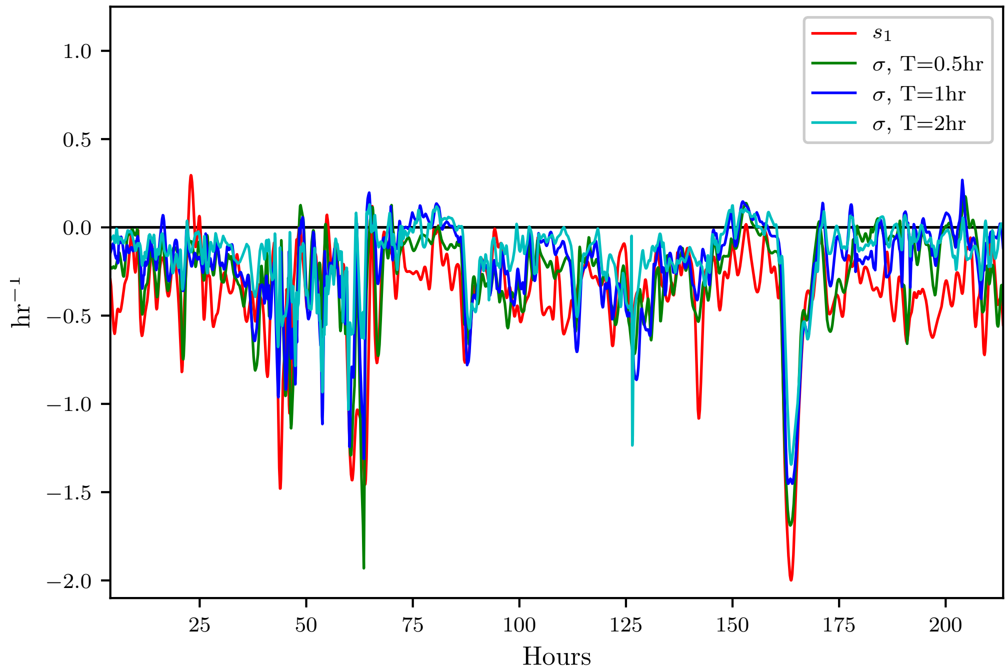

Figure 6: Comparison of the attraction rate with the 0.5, 1, and 2 hr backward-time FTLE from t=4 to t=215hrs. FTLE fields have been multiplied by -1 to offer better comparison of attraction.

rate be used to detect LCSs passing through an area, but it does a better job detecting attracting LCSs than the trajectory divergence rate does.

It should be noted that both the attraction and trajectory divergence rates seem to perform best at an area threshold of around 800-2000m and converge to random chance as the radius increases. We suspect that this is due to the spatial and temporal scales of the input data, 3km x 1hr grid spacing. We speculate that with a velocity field continuously defined in space and time, we would see continued improvement in the ROC curves as the threshold radius decreases. Unfortunately the analytic models currently used in the study of LCSs, such as the double gyre [29] and the Bickley jet [30], do not have the requisite spatial in-homogeneity necessary to reveal meaningful Eulerian structures.

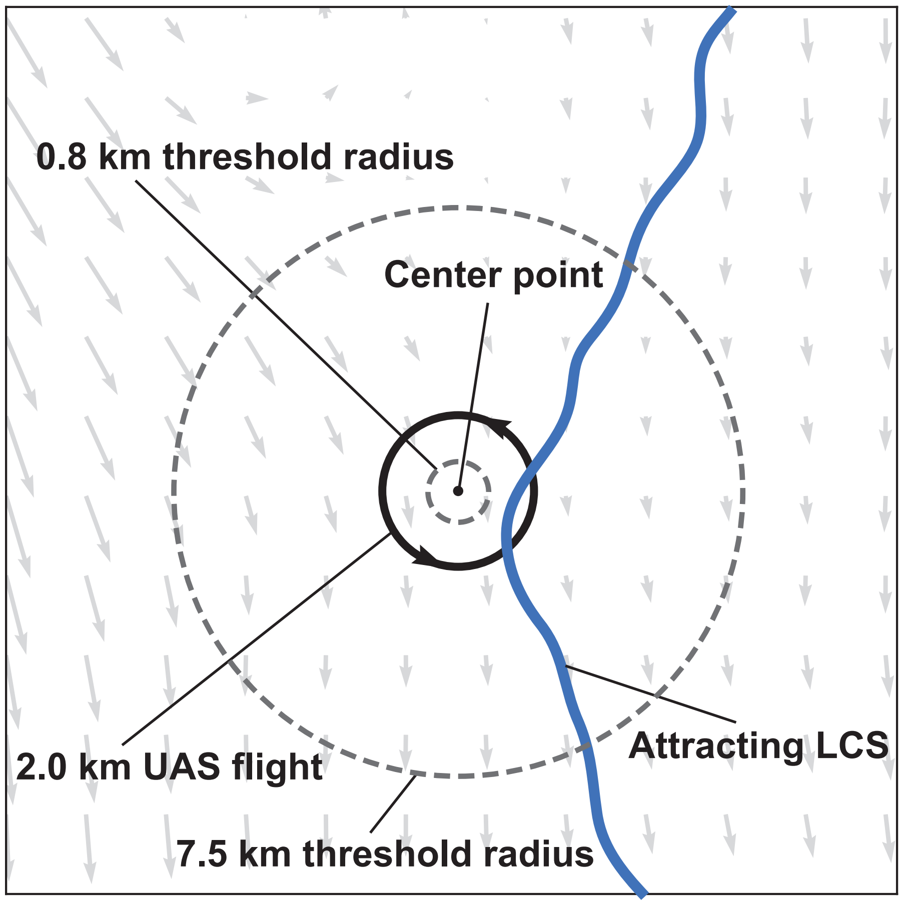

Figure 7: schematic of LCS detection. Two examples of threshold radii shown as dashed lines, with an attracting LCS falling withing one of threshold radius yet outside the other.

3.3 Inferring Lagrangian Dynamics from UAS measurements

In this section we examine how well the attraction rate, s_1, and the trajectory divergence rate, $\dot{\rho}$ as approximated from a UAS flight do at predicting Lagrangian dynamics, such as the passage of LCSs. Figure 10 shows ROC curves for the the trajectory divergence rate as calculated from a simulated 2km UAS flight. Once again we first masked trajectory divergence rate values > 0 to filter out repulsive indicators. After this, we threshold the from

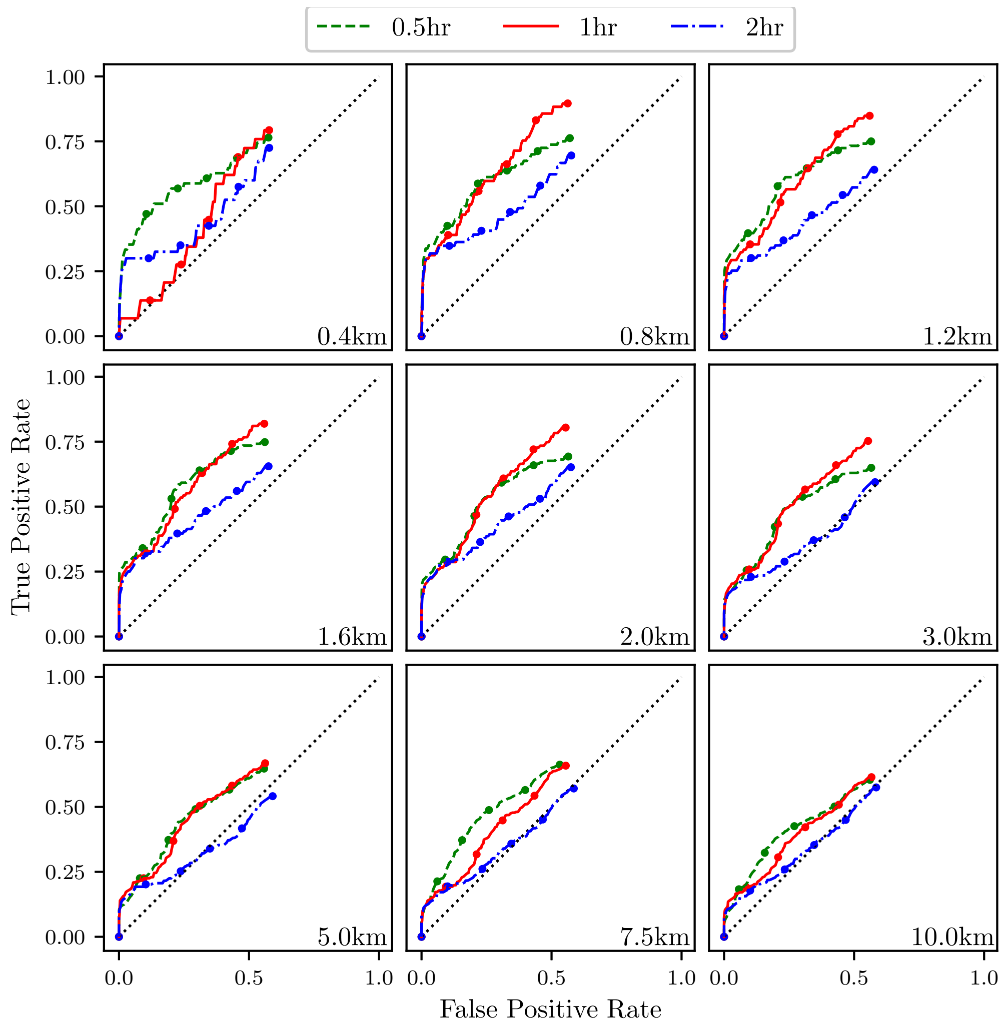

Figure 8: ROC curves for the trajectory divergence rate as measured at the center point ability to detect 90% percentile LCSs with integration times of 0.5 (green), 1 (red), and 2 (blue) hrs. Threshold radii are displayed in the lower left hand corner.

0%, upper right hand ride, to 100%, lower left hand corner. Every 20^{th} percentile is marked with a dot. Each subplot represents a different threshold radius, with radii ranging from 400m to 10km. Each color represents a different integration time for the LCSs, 0.5hr green, 1hr red, 2hr blue. These ROC curves show a striking resemblance to the ROC curves in figure 8. This

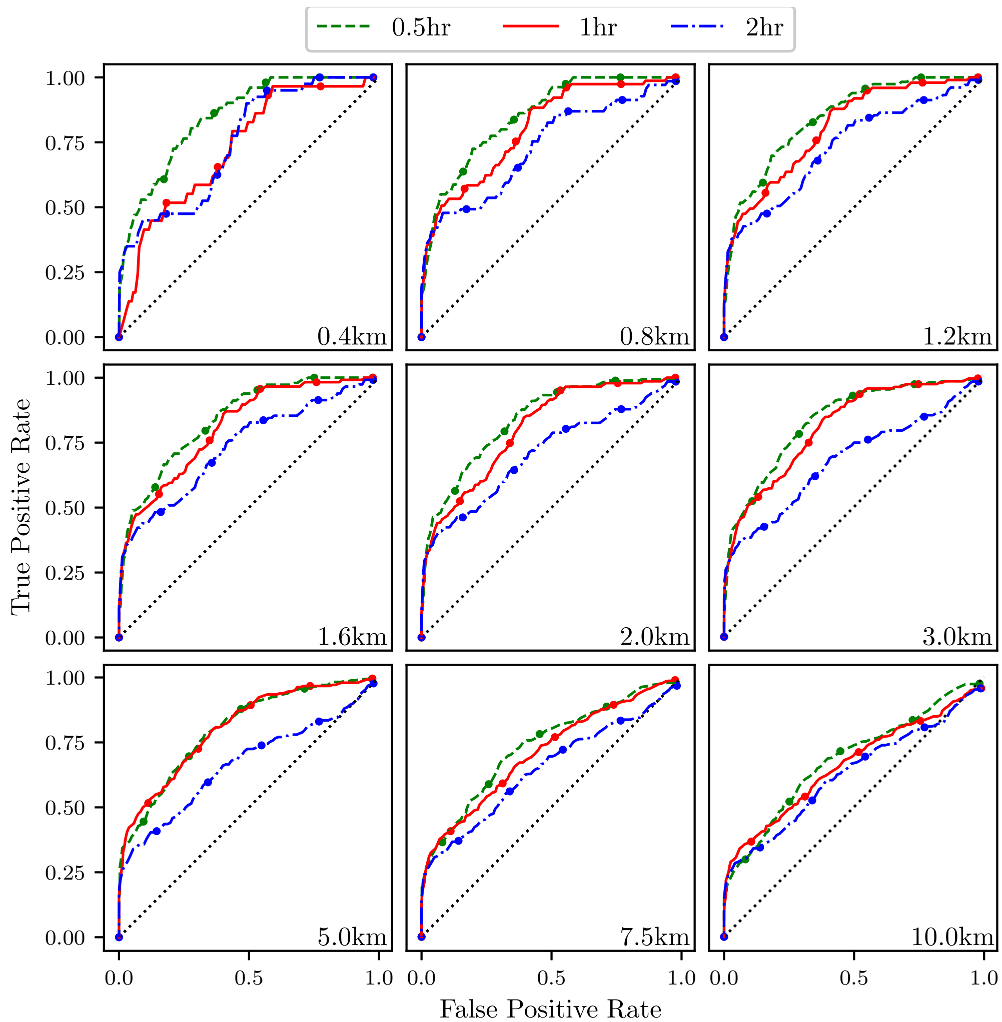

Figure 9: ROC curves for the attraction rate as measured at the center point ability to detect 90% percentile LCSs with integration times of 0.5 (green), 1 (red), and 2 (blue) hrs. Threshold radii are displayed in the lower left hand corner.

would indicate that the trajectory divergence rate as approximated from a UAS flight can indeed be used to detect LCSs passing through an area.

Figure 11 shows ROC curves for the attraction rate as calculated from a simulated 2km UAS flight. We threshold the attraction rate field from 0%, upper right hand corner, to 100%, lower left hand corner. Every 20^{th}

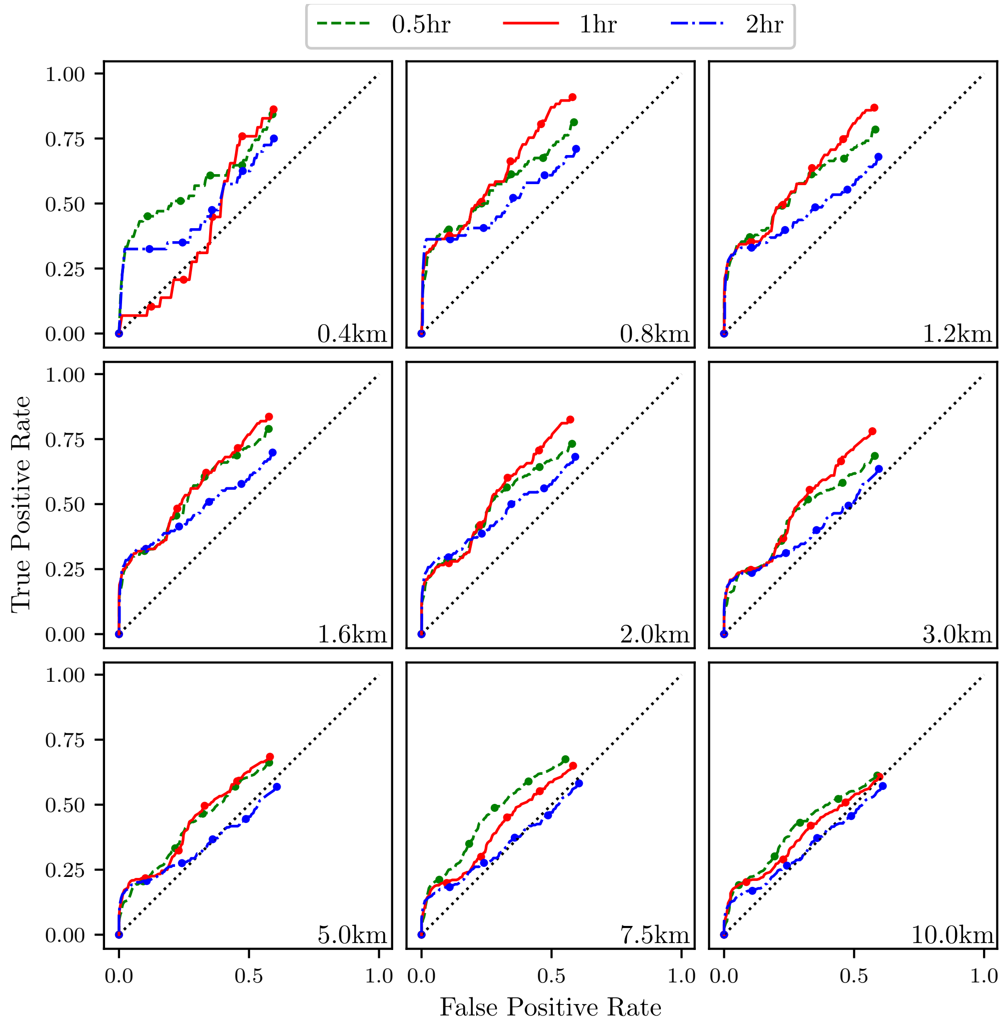

Figure 10: ROC curves for the trajectory divergence rate as measured from a 2km radius UAS simulation ability to detect 90% percentile LCSs with integration times of 0.5 (green), 1 (red), and 2 (blue) hrs. Threshold radii are displayed in the lower left hand corner.

percentile is marked with a dot. Each subplot represents a different threshold radius, with radii ranging from 400m to 10km. Each color represents a different integration time for the LCSs, 0.5hr green, 1hr red, 2hr blue. As before, these ROC curves closely resemble the ROC curves in figure 9. This would indicate that the attraction rate as approximated from a UAS flight can also be used to detect LCSs passing through an area.

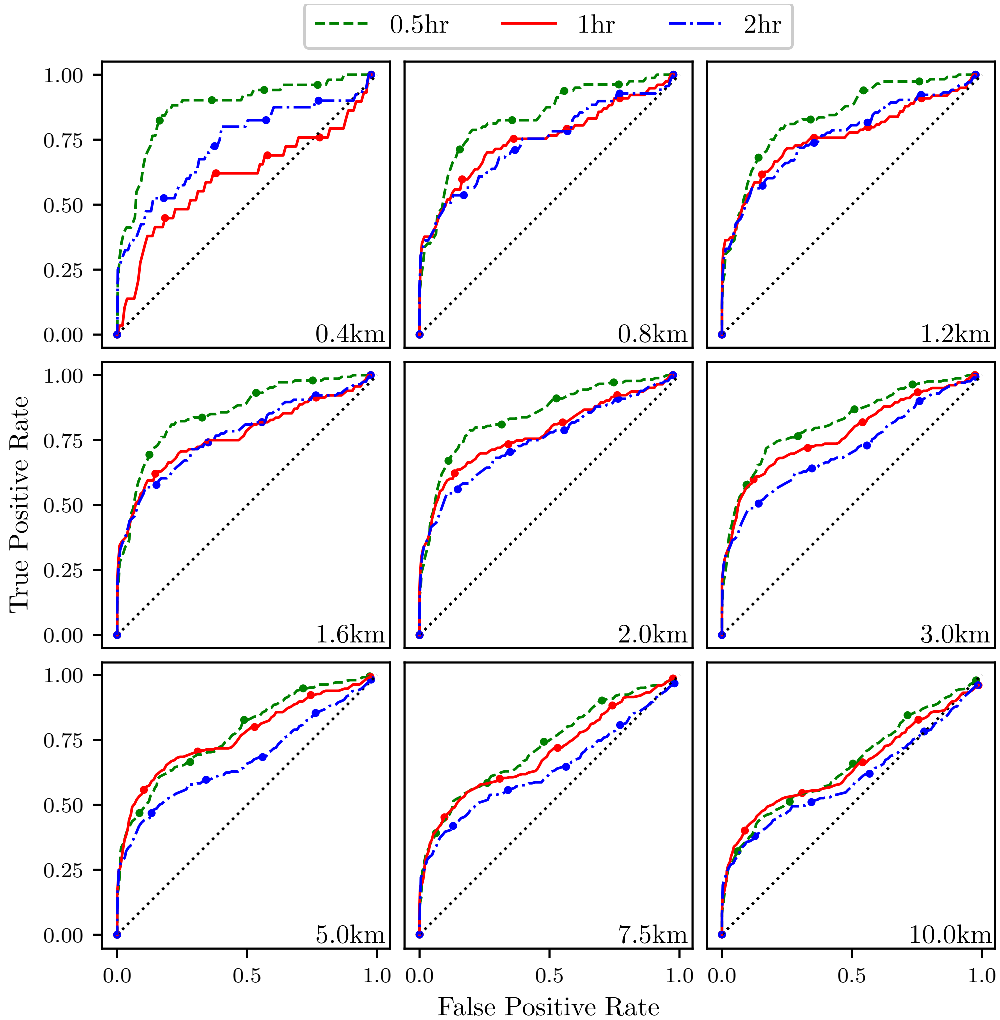

Figure 11: ROC curves for the attraction rate as measured from a 2km radius UAS simulation ability to detect 90% percentile LCSs with integration times of 0.5 (green), 1 (red), and 2 (blue) hrs. Threshold radii are displayed in the lower left hand corner.

The ROC curves in figures 10 and 11 indicate that both the trajectory divergence rate and the attraction rate as approximated from a UAS flight can be used to infer local Lagrangian dynamics. Furthermore, the attraction rate appears to be a much better indicator of passing attractive LCSs than the trajectory divergence rate. Interestingly, at around a 70-90% threshold the attraction rate as approximated by the UAS flight, figure 11, seems to outperforms the attraction rate at the center point, figure 9. We suspect that this is due to the fact that the UAS measurements are taking in information from a larger area and with these higher thresholds is filtering out the additional noise.

4 Conclusion

We have put forward a novel algorithm to approximate the gradient of a scalar field using measurements from a circular arc around a point. Using realistic atmospheric velocity data from the NAM 3km model, we applied this algorithm to circular trajectories restricted a 2D isosurface and simulated UAS flights in 3D, with radii ranging from 2km to 15km. From these results we approximated the trajectory divergence rate and the attraction rate for the center point of these paths. Comparing these approximations with the trajectory divergence rate and attraction rate at the center point, we found that both the flight and the circle gave nearly identical approximations. Furthermore, the approximations were very good for the smaller radii we looked, but even the larger radii approximations were able to pick up the trend of the trajectory divergence rate and attraction rate, though they underestimated the magnitude.

We have also examined the ability of Eulerian diagnostics, in particular the trajectory divergence and attraction rates, to infer Lagrangian dynamics. Using ROC curves, we first looked at the ability of the trajectory divergence rate and attraction rate, as measured at a point to detect the passage of LCSs within a threshold radius. We found that the attraction rate can be used as an effective tool to sense short term LCS passing by. We also found that the trajectory divergence rate, while performing better than chance, under performed the attraction rate. We then extended this to look at the trajectory divergence rate and attraction rate as approximated by a UAS flight. Once again we found that these Eulerian diagnostics, as approximated by a UAS flight, can be an effective tool for detecting LCSs passing through a sampling area.

This paper serves as a first step in real-time detection of LCSs in the atmosphere. It demonstrates that a fixed wing UAS can, in principle, be used to measure Eulerian diagnostics of a local atmospheric flow. These

Eulerian diagnostics can then be used to infer the Lagrangian dynamics of the local flow. Future work will apply this to real world data to detect actual atmospheric LCSs, evaluate the effects of sensor uncertainty on the accuracy of LCS detection, and extend this to the detection of pollutant specific LCSs, such as those found along atmospheric rivers [12].

A Flight Dynamic Model

The aircraft flight dynamic model comes from combining standard aircraft rigid-body equations [31] with Grauer and Morelli's Generic Global Aerodynamic model [32], modified for non-uniform wind. The important flight dynamic modeling assumptions are:

1. Earth is a flat, inertial reference.
2. The aircraft is a rigid body, symmetric about its longitudinal plane, with constant mass m.
3. For wind-aircraft interaction, the aircraft is a point "located" at it's center-of-mass.
4. The wind is described by a C^1-smooth kinematic vector field.
5. Aircraft thrust T is an instantaneously-controllable force acting nose-forward from the center-of-mass.
6. All parameters are invariant with altitude. (e.g. no altitudinal variation of density ρ, gravity g, ground-effect, etc.)

The resulting dynamic equations of motion are

$$\boldsymbol{R}_{BM}(\alpha)\begin{pmatrix} C_D(\ldots) \\ C_Y(\ldots) \\ C_L(\ldots) \end{pmatrix}\frac{1}{2}\rho\|\boldsymbol{V_r}\|^2 S + \begin{pmatrix} T_{\%}(\frac{T_{max}}{100\%}) \\ 0 \\ 0 \end{pmatrix} + \boldsymbol{R}_{BE}(\Theta)\begin{pmatrix} 0 \\ 0 \\ mg \end{pmatrix} = m\Big(\dot{\boldsymbol{V}} + (\boldsymbol{\omega}\times\boldsymbol{V})\Big), \tag{8}$$

$$\begin{bmatrix} b & 0 & 0 \\ 0 & \bar{c} & 0 \\ 0 & 0 & b \end{bmatrix}\begin{pmatrix} C_l(\ldots) \\ C_m(\ldots) \\ C_n(\ldots) \end{pmatrix}\frac{1}{2}\rho\|\boldsymbol{V_r}\|^2 S = \begin{bmatrix} I_{xx} & 0 & -I_{xz} \\ 0 & I_{yy} & 0 \\ -I_{xz} & 0 & I_{zz} \end{bmatrix}\dot{\boldsymbol{\omega}} + \Big(\boldsymbol{\omega}\times\begin{bmatrix} I_{xx} & 0 & -I_{xz} \\ 0 & I_{yy} & 0 \\ -I_{xz} & 0 & I_{zz} \end{bmatrix}\boldsymbol{\omega}\Big). \tag{9}$$

where the elipses on the aerodynamic coefficients remind the reader that these are functions of state variables, as given below in Equations 12 – 17. The symbol V is used for inertially-referenced velocity, and V_r is used for air-relative velocity. These dynamics are combined with standard translational and rotational kinematic equations

$$\dot{X} = \boldsymbol{R}_{EB}(\phi, \theta, \psi) \begin{pmatrix} u \\ v \\ w \end{pmatrix} = \boldsymbol{R}_{EB}(\Theta)\boldsymbol{V}, \tag{10}$$

$$\dot{\boldsymbol{\Theta}} = \begin{pmatrix} \dot{\phi} \\ \dot{\theta} \\ \dot{\psi} \end{pmatrix} = \begin{bmatrix} 1 & \sin\phi\tan\theta & \cos\phi\tan\theta \\ 0 & \cos\phi & -\sin\phi \\ 0 & \sin\phi\sec\theta & \cos\phi\sec\theta \end{bmatrix} \begin{pmatrix} p \\ q \\ r \end{pmatrix} = \boldsymbol{L}^{-1}(\phi, \theta)\boldsymbol{\omega}. \tag{11}$$

The aerodynamic coefficient expressions are from Equation 20 of Grauer and Morelli [32]

$$C_D = \theta_1 + \theta_2\alpha + \theta_3\alpha\tilde{q}_r + \theta_4\alpha\delta_e + \theta_5\alpha^2 + \theta_6\alpha^2\tilde{q}_r + \theta_7\alpha^2\delta_e + \theta_8\alpha^3 + \theta_9\alpha^3\tilde{q}_r + \theta_{10}\alpha^4, \tag{12}$$

$$C_Y = \theta_{11}\beta + \theta_{12}\tilde{p}_r + \theta_{13}\tilde{r}_r + \theta_{14}\delta_a + \theta_{14}\delta_r, \tag{13}$$

$$C_L = \theta_{16} + \theta_{17}\alpha + \theta_{18}\tilde{q}_r + \theta_{19}\delta_e + \theta_{20}\alpha\tilde{q}_r + \theta_{21}\alpha^2 + \theta_{22}\alpha^3 + \theta_{23}\alpha^4, \tag{14}$$

$$C_l = \theta_{24}\beta + \theta_{25}\tilde{p}_r + \theta_{26}\tilde{r}_r + \theta_{27}\delta_a + \theta_{28}\delta_r, \tag{15}$$

$$C_m = \theta_{29} + \theta_{30}\alpha + \theta_{31}\tilde{q}_r + \theta_{32}\delta_e + \theta_{33}\alpha\tilde{q}_r + \theta_{34}\alpha^2\tilde{q}_r + \theta_{35}\alpha^2\delta_e + \theta_{36}\alpha^3\tilde{q}_r + \theta_{37}\alpha^3\delta_e + \theta_{38}\alpha^4, \tag{16}$$

$$C_n = \theta_{39}\beta + \theta_{40}\tilde{p}_r + \theta_{41}\tilde{r}_r + \theta_{42}\delta_a + \theta_{43}\delta_r + \theta_{44}\beta^2 + \theta_{45}\beta^3. \tag{17}$$

In these equations $(\theta_1, \theta_2, \ldots \theta_{45})$ are the aircraft parameters, (α, β) are the standard aerodynamic angles, $(\tilde{p}_r, \tilde{q}_r, \tilde{r}_r)$ are wind-relative non-dimensionalized angular rates, and $(\delta_a, \delta_e, \delta_r)$ are aileron, elevator, and rudder deflections.

References

[1] P. Tallapragada, S. D. Ross, and D. G. Schmale. Lagrangian coherent structures are associated with fluctuations in airborne microbial populations. *Chaos*, 21:033122, 2011.

[2] DG Schmale and SD Ross. Highways in the sky: Scales of atmospheric transport of plant pathogens. *Annual Review of Phytopathology*, 53: 591–611, 2015.

[3] David G. Schmale and Shane D. Ross. High-flying microbes: Aerial drones and chaos theory help researchers explore the many ways that microorganisms spread havoc around the world. *Scientific American*, February:32–37, 2017.

[4] A. E. BozorgMagham, S. D. Ross, and D. G. Schmale III. Local finite-time lyapunov exponent, local sampling and probabilistic source and destination regions. *Nonlinear Processes in Geophysics*, 22(6):663–677, 2015.

[5] Jifeng Peng and Rorik Peterson. Attracting structures in volcanic ash transport. *Atmospheric environment*, 48:230–239, 2012.

[6] Wenbo Tang, Pak Wai Chan, and George Haller. Lagrangian coherent structure analysis of terminal winds detected by lidar. part i: Turbulence structures. *Journal of Applied Meteorology and Climatology*, 50(2):325–338, 2011.

[7] Marilena Kampa and Elias Castanas. Human health effects of air pollution. *Environmental pollution*, 151(2):362–367, 2008.

[8] Pope III C, Burnett RT, Thun MJ, and et al. Lung cancer, cardiopulmonary mortality, and long-term exposure to fine particulate air pollution. *JAMA*, 287(9):1132–1141, 2002. doi: 10.1001/jama.287.9.1132. URL + `http://dx.doi.org/10.1001/jama.287.9.1132`.

[9] Amir E BozorgMagham and Shane D Ross. Atmospheric lagrangian coherent structures considering unresolved turbulence and forecast uncertainty. *Communications in Nonlinear Science and Numerical Simulation*, 22(1):964–979, 2015.

[10] Carmine Senatore and Shane D Ross. Detection and characterization of transport barriers in complex flows via ridge extraction of the finite time lyapunov exponent field. *International Journal for Numerical Methods in Engineering*, 86(9):1163–1174, 2011.

[11] Jezabel Curbelo, Víctor José García-Garrido, Carlos Roberto Mechoso, Ana Maria Mancho, Stephen Wiggins, and Coumba Niang. Insights into the three-dimensional lagrangian geometry of the antarctic polar vortex. *Nonlinear Processes in Geophysics*, 24(3):379, 2017.

[12] Daniel Garaboa-Paz, Jorge Eiras-Barca, Florian Huhn, and Vicente Pérez-Muñuzuri. Lagrangian coherent structures along atmospheric rivers. *Chaos: An Interdisciplinary Journal of Nonlinear Science*, 25 (6):063105, 2015.

[13] Brent Knutson, Wenbo Tang, and Pak Wai Chan. Lagrangian coherent structure analysis of terminal winds: Three-dimensionality, intramodel variations, and flight analyses. *Advances in Meteorology*, 2015, 2015.

[14] Mattia Serra and George Haller. Objective eulerian coherent structures. *Chaos: An Interdisciplinary Journal of Nonlinear Science*, 26(5):053110, 2016.

[15] Gary K Nave Jr, Peter J Nolan, and Shane D Ross. Trajectory-free approximation of phase space structures using the trajectory divergence rate. *arXiv preprint arXiv:1705.07949v2*, 2018.

[16] D. N. Axford. On the accuracy of wind measurements using an inertial platform in an aircraft, and an example of a measurement of the vertical mesostructure of the atmosphere. *Journal of Applied Meteorology and Climatology*, 7:645–666, August 1968.

[17] Donald H. Lenschow and P. Spyers-Duran. Measurement techniques: Air motion sensing. Technical Report 23, National Center for Atmospheric Research, Boulder, CO, USA, 1989.

[18] NASA. Airborne science program website. `https://airbornescience.nasa.gov/`, 2017. accessed Jan 2017.

[19] Jack Elston, Brian Argrow, Maciej Stachura, Doug Weibel, Dale Lawrence, and David Pope. Overview of small fixed-wing unmanned aircraft for meteorological sampling. *Journal of Atmospheric and Oceanic Technology*, 32(1):97–115, 2015. doi: 10.1175/jtech-d-13-00236.1.

[20] Kasper T. Borup, Thor I. Fossen, and Tor A. Johansen. A nonlinear model-based wind velocity observer for unmanned aerial vehicles. *IFAC-PapersOnLine*, 49(18):276–283, 2016. doi: 10.1016/j.ifacol.2016.10.177. 10th IFAC Symposium on Nonlinear Control Systems.

[21] Matthew B. Rhudy, Yu Gu, Jason N. Gross, and Haiyang Chao. Onboard wind velocity estimation comparison for unmanned aircraft systems. *IEEE Transactions on Aerospace and Electronic Systems*, 53(1): 55–66, February 2017.

[22] F. Adhika Pradipta Lie and Demoz Gebre-Egziabher. Synthetic air data system. *Journal of Aircraft*, 50(4):1234–1249, July 2013.

[23] Jack W Langelaan, Nicholas Alley, and James Neidhoefer. Wind field estimation for small unmanned aerial vehicles. *Journal of Guidance, Control, and Dynamics*, 34(4):1016–1030, 2011. doi: 10.2514/1.52532.

[24] Brandon M Witte, Robert F Singler, and Sean CC Bailey. Development of an unmanned aerial vehicle for the measurement of turbulence in the atmospheric boundary layer. *Atmosphere*, 8(10):195, 2017. doi: 10.3390/atmos8100195.

[25] Andreas Wenz and Tor Arne Johansen. Estimation of wind velocities and aerodynamic coefficients for UAVs using standard autopilot sensors and a moving horizon estimator. In *International Conference on Unmanned Aircraft Systems (ICUAS)*, pages 1267–1276, Miami, FL, USA, June 2017. IEEE. doi: 10.1016/j.measurement.2018.01.027.

[26] Ronald Peikert, Benjamin Schindler, and Robert Carnecky. Ridge surface methods for the visualization of lagrangian coherent structures. In *Proceedings of the Ninth International Conference on Flow Dynamics, Sendai, Japan*, pages 206–207, 2012.

[27] Peter J Nolan and Shane D Ross. Mathematical properties of objective eulerian coherent structures and new method for vi-

sualization. *viXra preprint viXra:1810.0023*, Oct 2018. URL `http://vixra.org/abs/1810.0023`.

[28] Amir E BozorgMagham, Shane D Ross, and David G Schmale III. Real-time prediction of atmospheric lagrangian coherent structures based on forecast data: An application and error analysis. *Physica D: Nonlinear Phenomena*, 258:47–60, 2013.

[29] Shawn C Shadden, Francois Lekien, and Jerrold E Marsden. Definition and properties of lagrangian coherent structures from finite-time lyapunov exponents in two-dimensional aperiodic flows. *Physica D: Nonlinear Phenomena*, 212(3):271–304, 2005.

[30] II Rypina, MG Brown, FJ Beron-Vera, H Kocak, MJ Olascoaga, and IA Udovydchenkov. On the lagrangian dynamics of atmospheric zonal jets and the permeability of the stratospheric polar vortex. *Journal of the Atmospheric Sciences*, 64(10):3595–3610, 2007.

[31] Bernard Etkin. *Dynamics of Atmospheric Flight*. John Wiley & Sons, New York, 1972.

[32] Jared A. Grauer and Eugene A. Morelli. Generic global aerodynamic model for aircraft. *Journal of Aircraft*, 52(1):13–21, January 2015. doi: 10.2514/1.C032888.